nature physics

Article https://doi.org/10.1038/s41567-024-02444-w

Manipulation of chiral interface states in a moiré quantum anomalous Hall insulator

In the format provided by the authors and unedited

Table of contents

Supplementary Note 1: Carrier density, electric field, and filling factor

General expressions for carrier density n and out-of-plane displacement field D. Our STM/STS measurements feature a single-gate geometry (Fig. 1a) where the back-gate voltage V_G simultaneously controls the carrier density n and the out-of-plane electric displacement field D in the tMBLG stack. Both n and D are also modified by the presence of charge defects (either naturally occurring or induced via tip bias pulses) in the dielectric layers. The STM tip is intentionally prepared on a Cu(111) surface which has a work function similar to graphene to minimize tip-induced local gating effects that are known to be detrimental to the observation of correlated insulating states.[1] The absence of strong tip gating is evidenced by the undistorted spectroscopic features in Extended Data Fig. 1b. A straightforward electrostatic analysis yields:

$$n = \frac{\varepsilon_D \varepsilon_0 V_G}{e d_D} + \delta n \tag{1}$$

$$D = \frac{ne}{2} \tag{2}$$

where $\varepsilon_D \approx 3.6$ is the average out-of-plane dielectric constant of hBN and SiO_2, ε_0 is the vacuum permittivity, V_G is the back-gate voltage, e is the elementary charge, d_D = 315 nm is the thickness of the dielectric layers, and δn is the local density modification (see Supplementary Note 2 for further details).

Determining filling factor ν. We use two independent methods to convert V_G to the filling factor ν. First, we can calculate n using Eq. (1) and then derive ν through $\nu = n \cdot \frac{\sqrt{3}}{2} l_M^2$. The standard deviation of ν determined using this method can be up to ~5% due to uncertainties in ε_D and δn. Second, we also record the V_G values for which single-particle gaps appear in the dI/dV spectra (this happens at $\nu = \pm 4$) and then use linear interpolation to calculate ν for other V_G values (from ν we can then determine δn). This method is more accurate and has a standard deviation of ~1%. The ν values derived using these two methods are consistent with each other within our experimental error.

Comparison between STM/STS and transport parameters. Our STM/STS parameter space (which only involves one gate) is much more restricted compared to typical transport measurements of tMBLG involving dual-gate geometries where n and D can be independently controlled by varying top and bottom gate voltages.[2-5] Correlated insulating states have been reported to emerge at $\nu = 1, 2, 3$ over a finite range of D (sketched in Supplementary Fig. 1), demonstrating D-field tuning of correlation effects in tMBLG. In our experiment the D-field can only be directly proportional to n (Eq. (2)), and thus corresponds to a diagonal line-cut in the n−D plane.

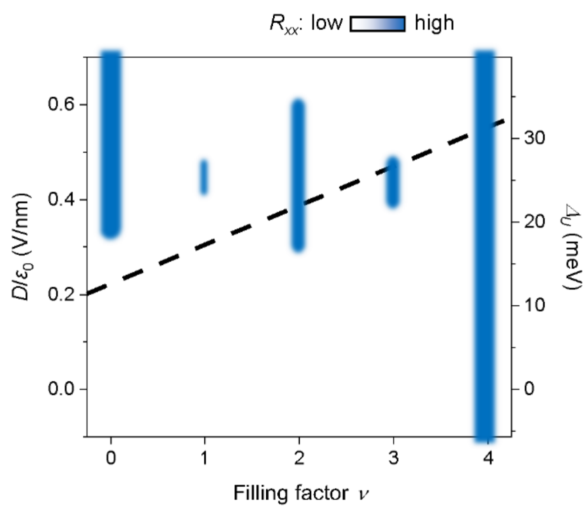

Supplementary Figure 1: STM/STS and transport parameter space correspondence. The dark blue regions indicate insulating phases in transport measurements (adapted from Ref. [2]). The dashed line is the STM/STS parameter space calculated using Eq. (3). Here D is the out-of-plane electric displacement field and Δ_U is the corresponding inter-layer potential difference.

Some care is needed to pinpoint the exact relationship between transport and STM/STS parameters. In transport the *D*-field creates a potential difference $\Delta_U = \frac{eDd_\mathrm{a}}{\varepsilon_\mathrm{eff}\varepsilon_0}$ between adjacent graphene layers (d_a = 0.33 nm is the inter-layer distance and ε_eff is the effective out-of-plane dielectric constant of tMBLG) that impacts the shape and alignment of flat bands and hence the correlated states of tMBLG. In STM/STS the different chemical environment of exposed carbon atoms in the top layer and those in contact with hBN in the bottom layer leads to an additional term Δ_{U0}, with the total inter-layer potential difference being

$$\Delta_U = \Delta_{U0} + \frac{eDd_\mathrm{a}}{\varepsilon_\mathrm{eff}\varepsilon_0} = \Delta_{U0} + \frac{ne^2 d_\mathrm{a}}{2\varepsilon_\mathrm{eff}\varepsilon_0} \tag{3}$$

Here Δ_{U0} and ε_eff can be estimated by comparing to theoretical simulations. A set of transport parameters and a set of STM/STS parameters are physically equivalent not when they have the same *D*, but when they lead to the same Δ_U. We can overlay the STM/STS parameter space as a dashed line in Supplementary Fig. 1, which touches the ν = 2 and the ν = 3 correlated insulating states while missing the ν = 1 one. This explains why correlation gaps appear in d*I*/d*V* at ν = 2, 3 but not at ν = 1 in our data (Extended Data Fig. 1b).

Supplementary Note 2: STM tip-pulse-induced quantum dot formation

Quantum dots were created following a protocol similar to that described in Ref. [6]:

1. A voltage V_G0 was applied to the back-gate, inducing an out-of-plane displacement field $D_0 = \frac{\varepsilon_\mathrm{D}\varepsilon_0 V_\mathrm{G0}}{d_\mathrm{D}}$ in the hBN dielectric.
2. The STM tip was lifted from the setpoint (V_Bias = –1 V, I_0 = 0.01 nA) by an offset of ΔZ = 1 nm to avoid possible damage to the graphene surface during the tip pulse.

3. A bias voltage pulse of 5 V was applied for a duration of 60 s. During this process the strong electric field generated by the pulse penetrates into hBN directly beneath the tip, resulting in enhanced defect field emission. The presence of gate-induced D_0 causes released electrons to drift either from the graphene electrode into hBN (when $V_{G0} > 0$) or from hBN into the graphene electrode (when $V_{G0} < 0$). This in turn results in a charging/discharging cascade during which charged defects effectively propagate across hBN all the way down to the SiO_2 interface.[7] Equilibrium is only reached when the extra carrier density δn completely screens D_0 (i.e., when $D_0 + \delta n\, e = 0$).
4. The charge carriers trapped at the hBN/SiO_2 interface are immobilized after removal of the bias voltage pulse, signifying formation of an n-type ($\delta n > 0$) or p-type ($\delta n < 0$) quantum dot.

Once created, tip-pulse-induced quantum dots are fairly stable and can persist for at least a few days at $T \approx 4$ K. They can be erased by repeating the above procedure while holding $V_{G0} =$ 0 V. The dot polarity can also be flipped by reversing the sign of V_{G0}. We note that reducing the hBN thickness would makes these quantum dots sharper and thus could be advantageous for device applications.

Supplementary Note 3: Gate-induced Chern domain interface depinning

We sometimes observe discontinuities in gate-dependent d*I*/d*V* density plots in the presence of a Chern domain interface, regardless of whether the underlying charge inhomogeneity occurs naturally (Extended Data Fig. 5e) or due to quantum dot formation (Fig. 4c, f). This phenomenon can be seen in Supplementary Fig. 2b−g where we present a series of d*I*/d*V* maps obtained at different gate voltages. The corresponding gate-dependent density plot at the location marked by a yellow “X” is shown in Supplementary Fig. 2a. Topological switching from $C = +2$ to $C = -2$ is observed in the density plot of Supplementary Fig. 2a when V_G is decreased from 44.9 V to 44.4 V (boxed region), but a closer inspection of the dI/dV maps (Supplementary Fig. 2b−g) reveals a change in behaviour when the marked position exits/enters a Chern insulating domain. At V_G = 44.9 V (Supplementary Fig. 2b) the scanned region is divided into a $C = -2$ domain on the left and a $C = +2$ domain on the right with the marked location being in a C = +2 insulating state. As V_G is gradually lowered to V_G = 44.6 V (Supplementary Fig. 2c−e) the $C = -2$ domain expands and the $C = +2$ domain shrinks, causing the interface to move rightward to the marked location. In the gate-dependent density plot of Supplementary Fig. 2a this interface movement is reflected as a continuous change from gapped behaviour (i.e., $C = +2$) to gapless behaviour (i.e., interface) as V_G is reduced.

When V_G is further reduced below 44.5 V (Supplementary Fig. 2f, g), however, the domain interface disappears suddenly (instead of moving smoothly rightward), thus leaving the entire region in an insulating $C = -2$ domain. Accordingly, the density plot of Supplementary Fig. 2a displays a discontinuous transition from gapless behaviour (i.e., interface) to gapped behaviour (i.e., $C = -2$). This type of abrupt depinning typically occurs only when a domain interface is leaving a region exhibiting a nearly constant charge density gradient (as can be seen in Supplementary Fig. 2). To avoid complications associated with this type of inhomogeneity-driven behaviour, the dI/dV mappings shown in the main text were all taken at gate voltages where the domain interface evolves continuously in regions of relatively constant charge density gradient.

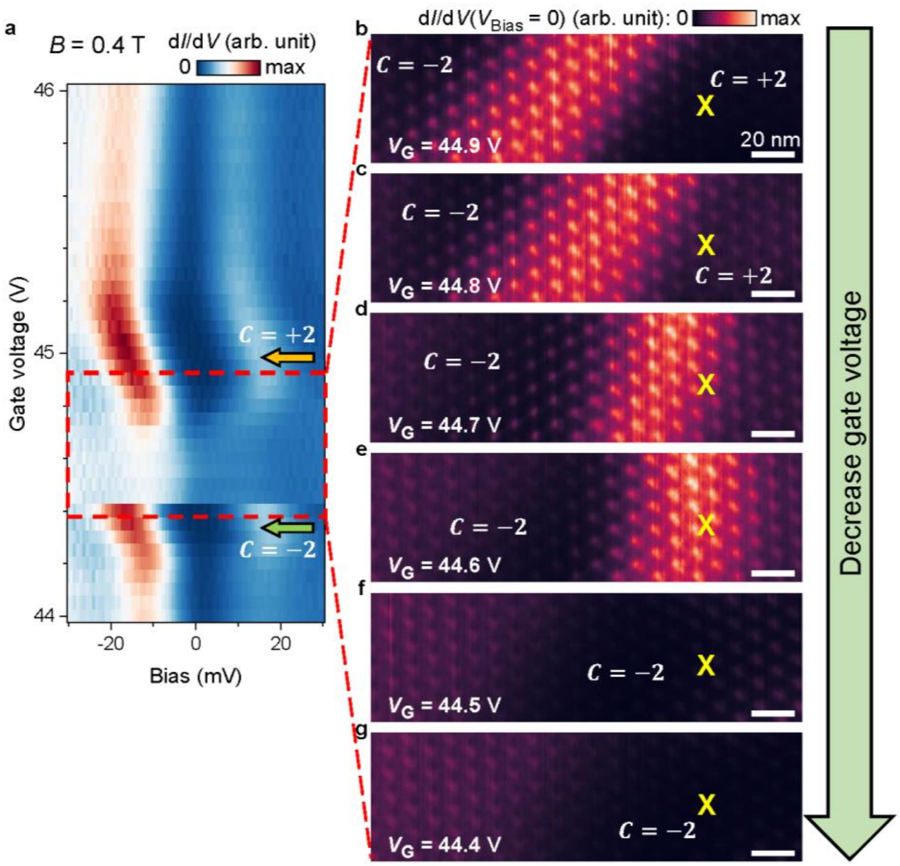

Supplementary Figure 2: Domain interface depinning and discontinuity in gate-dependent dI/dV**. a**, Gate-dependent dI/dV density plot for B = 0.4 T obtained at the location marked in **b**–**g** (same data as Extended Data Fig. 5e). Orange and green arrows indicate C = +2 and C = –2 gaps. Red dashed box marks the gate range of dI/dV maps in **b**–**g**. **b**–**g**, dI/dV maps of the same area as Extended Data Fig. 5a at B = 0.4 T and V_{Bias} = 0 mV for **b** V_{G} = 44.9 V, **c** V_{G} = 44.8 V, **d** V_{G} = 44.7 V, **e** V_{G} = 44.6 V, **f** V_{G} = 44.5 V, and **g** V_{G} = 44.4 V. Spectroscopy parameters: modulation voltage ΔV_{RMS} = 1 mV; setpoint V_{Bias} = –60 mV, I_0 = 0.5 nA for **a**; setpoint V_{Bias} = –300 mV, I_0 = 0.2 nA and tip height offset ΔZ = –0.2 nm for **b**–**g**.

Supplementary Note 4: Theoretical model and calculations

We model the moiré mini-bands in tMBLG using a continuum Hamiltonian in momentum space.[8-10] Here the monolayer graphene is modelled using a two-band tight-binding model with t_0 = 2.8 eV and the Bernal-stacked bilayer is modelled using a four-band model with t_0 = 2.61 eV, t_1 = 0.361 eV, t_3 = 0.283 eV, t_4 = 0.138 eV, and Δ = 0.015 eV.[11] The bilayer is rotated by an angle θ = 1.25° and hybridized with the monolayer with intra-sublattice strength w_{AA} = 87.75 meV and inter-sublattice strength w_{AB} = 117 meV. We also include a potential difference Δ_U = 26.6 meV between adjacent graphene layers to account for the gate-induced out-of-plane electric field as well as the asymmetry between top and bottom layers due to the presence of the hBN substrate (see Supplementary Note 1).[12] The moiré Bravais vectors are given by $\mathbf{a}_1 = l_\mathrm{M}\left(\frac{\sqrt{3}}{2}, \frac{1}{2}\right)$, $\mathbf{a}_2 = l_\mathrm{M}(0, 1)$ (some of our theoretical plots (e.g., Extended Data Fig. 4d) have their coordinates rotated so that they better align with experimental images).

To calculate real-space LDOS, we construct a tight-binding model in hybrid coordinate–momentum space. Our basis states are obtained by performing a 1D Fourier transformation of Bloch wavefunctions within a spin- and valley-resolved moiré mini-band so that they become localized Wannier orbitals in the x direction while remaining eigenstates of k_y[13-15] (we choose a gauge where these basis states are maximally localized in x [16]). Each basis state is labelled by an x-direction unit cell index n and a y-direction momentum index k_y (16 discrete k_y values in the 1D Brillouin zone $-\frac{\pi}{a_{2y}} \leq k_y < \frac{\pi}{a_{2y}}$ are used in our simulations where a_{2y} is the y component of $\mathbf{a}_2$). The x expectation value of a basis state is $\langle x \rangle_{k_y,n} = n a_{1x} + P_x(k_y)$ where a_{1x} is the x component of $\mathbf{a}_1$ and $P_x(k_y)$ is the average position (i.e., center of mass) of the Wannier function along x relative to the centre of the unit cell.

To capture the valley polarization reversal, we assume that each basis state feels an effective energy offset $m(x)$ depending on its x expectation value. Our full Hamiltonian thus reads

$$H = \sum_{k_y,n,n'} t_{k_y,n,n'} c^{\dagger}_{k_y,n} c_{k_y,n'} + \sum_{k_y,n} m\left(x = na_{1x} + P_x(k_y)\right) c^{\dagger}_{k_y,n} c_{k_y,n} \tag{4}$$

where the hopping coefficients $t_{k_y,n,n'}$ are obtained from the Fourier transform of the momentum-space continuum Hamiltonian for bulk tMBLG. Assuming that the system retains the same spin polarization across the domain interface (to minimize the spin Zeeman energy in the applied out-of-plane *B*-field), we model the energy offset *m*(*x*) for basis states from the $K_+ \uparrow$ sub-band as

$$m(x) = \begin{cases} +\mathcal{E}_0 & x < -\frac{\xi}{2} \\ -\frac{2\mathcal{E}_0 x}{\xi} & -\frac{\xi}{2} \leq x < +\frac{\xi}{2} \\ -\mathcal{E}_0 & +\frac{\xi}{2} \leq x \end{cases} \tag{5}$$

as shown by the solid orange line in Supplementary Fig. 3. These states are first centred at $+\mathcal{E}_0$ (where they remain empty) in a *C* = –2 domain ($x < -\frac{\xi}{2}$) and ends up centered at $-\mathcal{E}_0$ (where they are filled) in a *C* = +2 domain ($x \geq \frac{\xi}{2}$). As the interface is crossed *m*(*x*) shifts linearly from $+\mathcal{E}_0$ to $-\mathcal{E}_0$ over a domain wall width = ξ (i.e., $-\frac{\xi}{2} \leq x < +\frac{\xi}{2}$). Basis states from the $K_- \uparrow$ sub-band, on the other hand, have an opposite energy offset profile given by –*m*(*x*) which reflects an upward energy shift from left to right (solid green line in Supplementary Fig. 3). Here $2\mathcal{E}_0 = 30$ meV is extracted from the separation between LB and UB features in the experimental d*I*/d*V* (Fig. 2d, f) and ξ is treated as a fitting parameter (this is the only parameter in the model that is not initially constrained by experimental values). We take $m(x) \equiv -\mathcal{E}_0$ for $K_+ \downarrow$ and $K_- \downarrow$ sub-bands since they remain at the LB energy and do not shift across the domain interface (orange and green dashed lines).

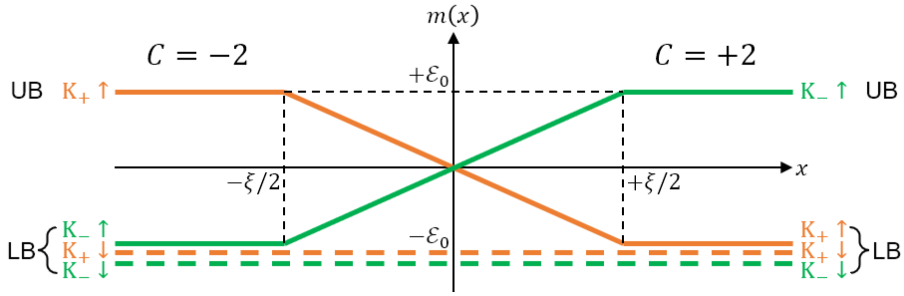

Supplementary Figure 3: Energy offset profiles for different spin- and valley-resolved sub-bands. $2\mathcal{E}_0 = 30$ meV is the exchange-induced energy separation between occupied (i.e. LB) and unoccupied (i.e., UB) sub-bands in the tMBLG bulk. ξ is the Chern domain wall width.

The band structures plotted in Extended Data Fig. 10a, c are obtained by diagonalizing the Hamiltonian of Eq. (4) for spin-up electrons at each k_y (spin-down electrons do not contribute to the interface states). The LDOS plots shown in Fig. 2g, Extended Data Fig. 4d–f, and Extended Data Fig. 10b, d are obtained by computing the charge density of all eigenstates and convolving them with a Lorentzian of width η = 3 meV to model various broadening mechanisms. The LDOS is always projected onto the topmost graphene layer to enable comparison with the experimental dI/dV. We note that our model is reminiscent of edge state formation in an integer quantum Hall (IQH) insulator[17] with $m(x)$ playing the role of the confining potential and its spatial gradient (i.e., the effective electric force field) $\left|\frac{\Delta m}{\Delta x}\right| = \frac{2\mathcal{E}_0}{\xi}$ controlling the group velocity of the chiral edge modes. Unlike the IQH case, however, here the valley polarization of tMBLG electronic states and its reversal across the Chern domain interface are purely interaction-driven effects. Future theoretical investigations will be required to provide a more accurate description of $m(x)$ and its dependence on experimental parameters.

References

1 Farahi, G. *et al.* Broken symmetries and excitation spectra of interacting electrons in partially filled Landau levels. *Nature Physics* (2023). https://doi.org/10.1038/s41567-023-02126-z

2 Polshyn, H. *et al.* Electrical switching of magnetic order in an orbital Chern insulator. *Nature* **588**, 66-70 (2020). https://doi.org/10.1038/s41586-020-2963-8

3 Chen, S. *et al.* Electrically tunable correlated and topological states in twisted monolayer–bilayer graphene. *Nature Physics* **17**, 374-380 (2021). https://doi.org/10.1038/s41567-020-01062-6

4 Xu, S. *et al.* Tunable van Hove singularities and correlated states in twisted monolayer–bilayer graphene. *Nature Physics* **17**, 619-626 (2021). https://doi.org/10.1038/s41567-021-01172-9

5 He, M. *et al.* Competing correlated states and abundant orbital magnetism in twisted monolayer-bilayer graphene. *Nature Communications* **12**, 4727 (2021). https://doi.org/10.1038/s41467-021-25044-1

6 Velasco, J. *et al.* Nanoscale Control of Rewriteable Doping Patterns in Pristine Graphene/Boron Nitride Heterostructures. *Nano Letters* **16**, 1620-1625 (2016). https://doi.org/10.1021/acs.nanolett.5b04441

7 Shi, W. *et al.* Reversible writing of high-mobility and high-carrier-density doping patterns in two-dimensional van der Waals heterostructures. *Nature Electronics* **3**, 99-105 (2020). https://doi.org/10.1038/s41928-019-0351-x

8 Bistritzer, R. & MacDonald, A. H. Moiré bands in twisted double-layer graphene. *Proceedings of the National Academy of Sciences* **108**, 12233-12237 (2011). https://doi.org/10.1073/pnas.1108174108

9 Park, Y., Chittari, B. L. & Jung, J. Gate-tunable topological flat bands in twisted monolayer-bilayer graphene. *Physical Review B* **102**, 035411 (2020). https://doi.org/10.1103/PhysRevB.102.035411

10 Rademaker, L., Protopopov, I. V. & Abanin, D. A. Topological flat bands and correlated states in twisted monolayer-bilayer graphene. *Physical Review Research* **2**, 033150 (2020). https://doi.org/10.1103/PhysRevResearch.2.033150

11 Jung, J. & MacDonald, A. H. Accurate tight-binding models for the π bands of bilayer graphene. *Physical Review B* **89**, 035405 (2014). https://doi.org/10.1103/PhysRevB.89.035405

12 Zhang, C. *et al*. Local spectroscopy of a gate-switchable moiré quantum anomalous Hall insulator. *Nature Communications* **14**, 3595 (2023). https://doi.org/10.1038/s41467-023-39110-3

13 Marzari, N., Mostofi, A. A., Yates, J. R., Souza, I. & Vanderbilt, D. Maximally localized Wannier functions: Theory and applications. *Reviews of Modern Physics* **84**, 1419-1475 (2012). https://doi.org/10.1103/RevModPhys.84.1419

14 Kang, J. & Vafek, O. Non-Abelian Dirac node braiding and near-degeneracy of correlated phases at odd integer filling in magic-angle twisted bilayer graphene. *Physical Review B* **102**, 035161 (2020). https://doi.org/10.1103/PhysRevB.102.035161

15 Soejima, T., Parker, D. E., Bultinck, N., Hauschild, J. & Zaletel, M. P. Efficient simulation of moiré materials using the density matrix renormalization group. *Physical Review B* **102**, 205111 (2020). https://doi.org/10.1103/PhysRevB.102.205111

16 Marzari, N. & Vanderbilt, D. Maximally localized generalized Wannier functions for composite energy bands. *Physical Review B* **56**, 12847-12865 (1997). https://doi.org/10.1103/PhysRevB.56.12847

17 Halperin, B. I. Quantized Hall conductance, current-carrying edge states, and the existence of extended states in a two-dimensional disordered potential. *Physical Review B* **25**, 2185-2190 (1982). https://doi.org/10.1103/PhysRevB.25.2185